nature communications

Article

https://doi.org/10.1038/s41467-025-62807-6

Hierarchical luminescence center coupling enables time-dependent phosphorescence color from self-protective carbonized polymer dots

Received: 24 March 2025

Accepted: 31 July 2025

Published online: 12 August 2025

Check for updates

Meichao Shi[1], Qian Gao[1], Mingxing Chen[2], Ziwen Lv[1], Jun Rao[1], Gegu Chen[1], Baozhong Lü[1] ✉, Wei Qi[3], Junli Ren[4] & Feng Peng[1,5] ✉

Time-dependent phosphorescence color is attractive for various applications; however, the modulation mechanism of multiple luminescence centers is still confused. Herein, we proposed a hierarchical luminescence center coupling strategy to develop self-protective xylan carbonized polymer dots with time-dependent phosphorescence color. When using 1,3-diaminopropane as the cross-linker, the polymer dots feature a highly stable and rigid architecture, the clusterization-triggered phosphorescence of which is fully exploited to form hierarchical core–shell phosphorescence centers with different afterglow colors. The core with blue afterglow is dominant at first, and the shell with yellow-green afterglow becomes dominant over time, leading to a typical time-dependent phosphorescence color evolution with large color contrast. The eco-friendly xylan carbonized polymer dots with high contrast time-dependent phosphorescence color can be used for advanced dynamic information encryption and anti-counterfeiting. This work provides an effective method to achieve time-dependent phosphorescence color, and gives insights into the phosphorescence mechanism of carbonized polymer dots.

Long-lived room temperature phosphorescence (RTP) materials exhibit persistent luminescence after ceasing the excitation light source[1–3]. The afterglow can last for several seconds to even hours. Thanks to the advantages of long lifetime, large Stokes shift, elimination of background fluorescence interference, and high signal-to-noise ratio[4–8], RTP materials have attracted extensive attention in the fields of optoelectronic devices, anti-counterfeiting, information encryption, sensors, bioimaging, and so on[9–18]. Currently, organic RTP materials with the advantages of low cost, good processability, and easy functionality have been developed to replace inorganic RTP materials containing precious metals or rare elements, because the inorganic ones face the problems of poor biocompatibility, high toxicity, harsh processing conditions, and high cost[19–21]. Two principles should be executed for realizing long-lived RTP in organic systems: 1) improving the intersystem crossing (ISC) between the excited singlet state (S_1) and a triplet state (T_n); 2) and suppressing the nonradiative transitions of the triplet excitons. Strategies to develop organic RTP materials include H-aggregation, carbon dots (CDs) engineering, crystal engineering, rigid matrix encapsulation, etc[22–26]. Despite the rapid development of organic RTP materials, most of them exhibit static

[1]Beijing Key Laboratory of Lignocellulosic Chemistry, MOE Engineering Research Center of Forestry Biomass Materials and Bioenergy, College of Materials Science and Technology, Beijing Forestry University, Beijing 100083, China. [2]Analytical Instrumentation Center of Peking University, Peking University, Beijing 100871, China. [3]Guangzhou Institute of Energy Conversion, Chinese Academy of Sciences, Guangzhou 510640, China. [4]State Key Laboratory of Pulp and Paper Engineering, South China University of Technology, Guangzhou 510641, China. [5]State Key Laboratory of Efficient Production of Forest Resources, Beijing 100083, China. ✉e-mail: lvbaozhong@bjfu.edu.cn; fengpeng@bjfu.edu.cn

phosphorescence color, limiting their practical applications. Therefore, there is an urgent need to develop dynamic color-changing RTP materials responding to conditions such as excitation wavelength, delay time, heat, etc[10,27,28].

Time-dependent phosphorescence color (TDPC) materials, whose afterglow color can be altered in the time dimension, possess very high security level in the application of dynamic information encryption and multi-mode anti-counterfeiting. Compared with excitation-dependent RTP materials, TDPC materials require only a single wavelength of excitation light source to achieve color change, reducing the complexity of light source design and making them more suitable for practical application such as bio-imaging and information encryption[29,30]. There are more than two afterglow colors in TDPC materials that can be detected by human eye in the afterglow emission process. Apparently, the wide color change and long afterglow duration are favorite features of TDPC. TDPC materials provide additional color channels within the limited time dimension, which allow for higher levels of information security[31–35]. Multiple emissive species with different phosphorescence colors and lifetimes are key to achieving TDPC[31,36,37]. Unfortunately, most of TDPC materials currently suffer from tedious synthesis processes and unsharp color change. Moreover, the development of TDPC materials is still in infancy. Developing a simple strategy to give TDPC properties to existing RTP materials is essential, although difficult in theory and in practice.

As an emerging metal-free organic RTP material, carbonized polymer dots (CPDs) are of great advantages including wide range of raw material sources, lost toxicity, low cost, and eco-friendly property[38,39]. CPDs feature core-shell hierarchical structures, where the carbon core is composed of a highly cross-linked network with or without slight carbonization, and the shell layer consists of an abundance of polymer chains or functional groups, which are usually derived from incompletely carbonized precursors[40]. Traditional CPDs are developed only to active the static single color RTP via the pronounced crosslink-enhanced emission (CEE) effect[2]. However, several groups, including ourselves, have reported TDPC materials from CDs and CPDs. For example, Ren et al. reported a TDPC material by printing CDs on paper[37]. Zheng et al. demonstrated a time-dependent dynamic RTP system by confining silane-functionalized CDs in a silica matrix[41]. Yang et al. have reported a time-dependent RTP CPDs regulated by hydrochloric acid[33]. Shi et al. reported that structural defects of inorganic NaCl could trigger the TDPC performance of CDs with a single emission center[35]. Zhang et al. demonstrated an alkali metal-mediated ionic bonding strategy for achieving TDPC CPDs[34]. Our group reported that matrix confinement could activate the core-shell phosphorescence centers of CPDs to realize TDPC[42]. Although breakthrough results have been achieved, the reported CDs need to be confined in the rigid matrix or extra components need to be introduced in the CDs to activate multiple emissive centers and subsequent TDPC. Consequently, on one hand, it will increase the complexity of material preparation and the risk of result reproducibility; on the other hand, the multi-component system is not conducive to uncover the structure-TDPC performance relationship of CPDs. Thus, the realization of TDPC on self-protective CPDs without any doping is of great significance for TDPC mechanism interpretation as well as the structure innovation of the TDPC materials.

As a proof of concept, we elaborately designed and prepared a series of xylan-based CPDs. Xylan was chosen as the precursors because we have proven that it can provide high-performance clusterization-triggered phosphorescence (CTP). Moreover, xylan, a linear chain hemicellulose, is a byproduct from paper or viscose fiber mills. Xylan is highly low cost and environmentally friendly compared with other petroleum-based polymers. Xylan was firstly etherified to form carboxymethylated xylan (CMX), which could be crosslinked by alkyl diamines to form X-CPDs$_{-n}$ (n represents the number of carbon atoms of alkyl diamine) with a hierarchical core-shell structure with the polymer structure outside and cross-linked core inside (Fig. 1a). Next, the core–shell phosphorescence centers of X-CPDs were precisely balanced and stabilized by regulating the length of diamine cross-linker, consequently regulating the structural rigidity for CTP and ultimately modulating the TDPC performance. Specifically, short alkyl diamine ($n = 2$) will lead to the excessive carbonization of the cross-linked core, obstructing the CTP; overlong alkyl diamine ($n \geq 4$) will cause free volume for free movement of molecules, enhancing the nonradiative transition (Fig. 1b). Thus, the above X-CPDs$_{-n}$ ($n = 2$, 4-8) only show yellow-green phosphorescence originating from the low-energy surface oxide triplet state emissive clusters at room temperature (Fig. 1b, c). Suitable alkyl diamine ($n = 3$) activates the high-energy blue phosphorescence center of N-related cross-linked core. Thus, the core-related blue phosphorescence center and shell-related yellow-green phosphorescence center coexist via hierarchical luminescence center coupling, and the afterglow of self-protective X-CPDs$_{-3}$ shows a change from blue to blue-green then to yellow-green within 1 s at room temperature (Fig. 1b, c). The TDPC of X-CPDs$_{-3}$ was then successfully applied in 3D crafts and advanced dynamic information encryption. The work provides an efficient method to prepare TDPC self-protective CPDs without any rigid matrix confinement nor extra component, and uncovers the structure-TDPC performance relationship of CPDs.

Results

Preparation and characterization of X-CPDs$_{-n}$

X-CPDs$_{-n}$ ($n = 2$–8) were prepared by hydrothermal reaction using CMX and various alkyl diamines as precursors. X-CPDs$_{-2}$ powders show the deepest color, while X-CPDs$_{-3}$ and X-CPDs$_{-n}$ ($n = 4$–8) powders show creamy white or pale-yellow appearance (Supplementary Fig. 1). Transmission electron microscopy (TEM) images reveal the formation of X-CPDs$_{-n}$ ($n = 2$–8) with well-dispersed quasi-spherical shapes and similar particle sizes (3–4 nm), suggesting that the length of alkyl chains have no significant effect on the morphology and size of the prepared CPDs (Fig. 2a, b). There are but not many lattice fringes can be observed in X-CPDs$_{-n}$ ($n = 2$–8) under high-resolution TEM (HR-TEM) images, proving inside cores are highly cross-linked polymer structures with a moderate degree of carbonization (Supplementary Fig. 2). Furthermore, the XRD patterns of X-CPDs$_{-n}$ ($n = 2$–8) exhibit broad diffraction peaks at 12.4°, 19.5°, 30.2° and 40.7° similar to CMX, suggesting the reserved amorphous CMX polymer structures are dominant in X-CPDs (Fig. 2c). In the Raman spectra, two peaks at 1387 cm^{-1} and 1584 cm^{-1} attributed to D band and G band are observed, declaring X-CPDs$_{-n}$ ($n = 2$–8) possess sp^3 hybridized amorphous carbon and sp^2 hybridized graphitic crystalline domains (Supplementary Fig. 3). The area(D)/area(G) of X-CPDs$_{-n}$ ($n = 2$–8) are determined to be 3.19, 4.43, 3.04, 3.48, 2.9, 2.76, and 3.01, respectively. Area(D)/area(G) indicates the ratio of unconjugated/conjugated domains, also suggesting the amorphous unconjugated structures are dominant. Nuclear magnetic resonance (NMR) spectra were used to gain further insight into the structure of X-CPDs$_{-n}$ ($n = 2$–8). As shown in Fig. 2d, the ^{13}C NMR spectra indicate that X-CPDs$_{-n}$ ($n = 2$–8) retain the carbon skeleton of CMX[42,43]. The carbon signal of N-CH_2 present in X-CPDs$_{-n}$ ($n = 2$–8) proves that CMX and diamines with different alkyl chain lengths have been successfully cross-linked to form amide or imine bonds. As shown in Supplementary Figs. 4–10, the ^{1}H NMR signals of X-CPDs$_{-n}$ ($n = 2$–8) further prove the existence of cross-linking sites of N-CH_2 units. Moreover, all the signals observed in the ^{1}H and ^{13}C NMR spectra could be assigned according to the simplified cross-linking unit[44–46]. The above results verify that X-CPDs feature CMX structure outside and highly crosslinked N-contained rigid network inside (Fig. 1a). As shown in Fig. 2e, the Fourier transform infrared (FTIR) spectra show that X-CPDs$_{-n}$ ($n = 2$–8) all have similar characteristic peaks, the peaks at 3410 and 1467 cm^{-1} can be attributed to N-H stretching vibrations; while the bands at 1645 cm^{-1} can be ascribed to

https://doi.org/10.1038/s41467-025-62807-6

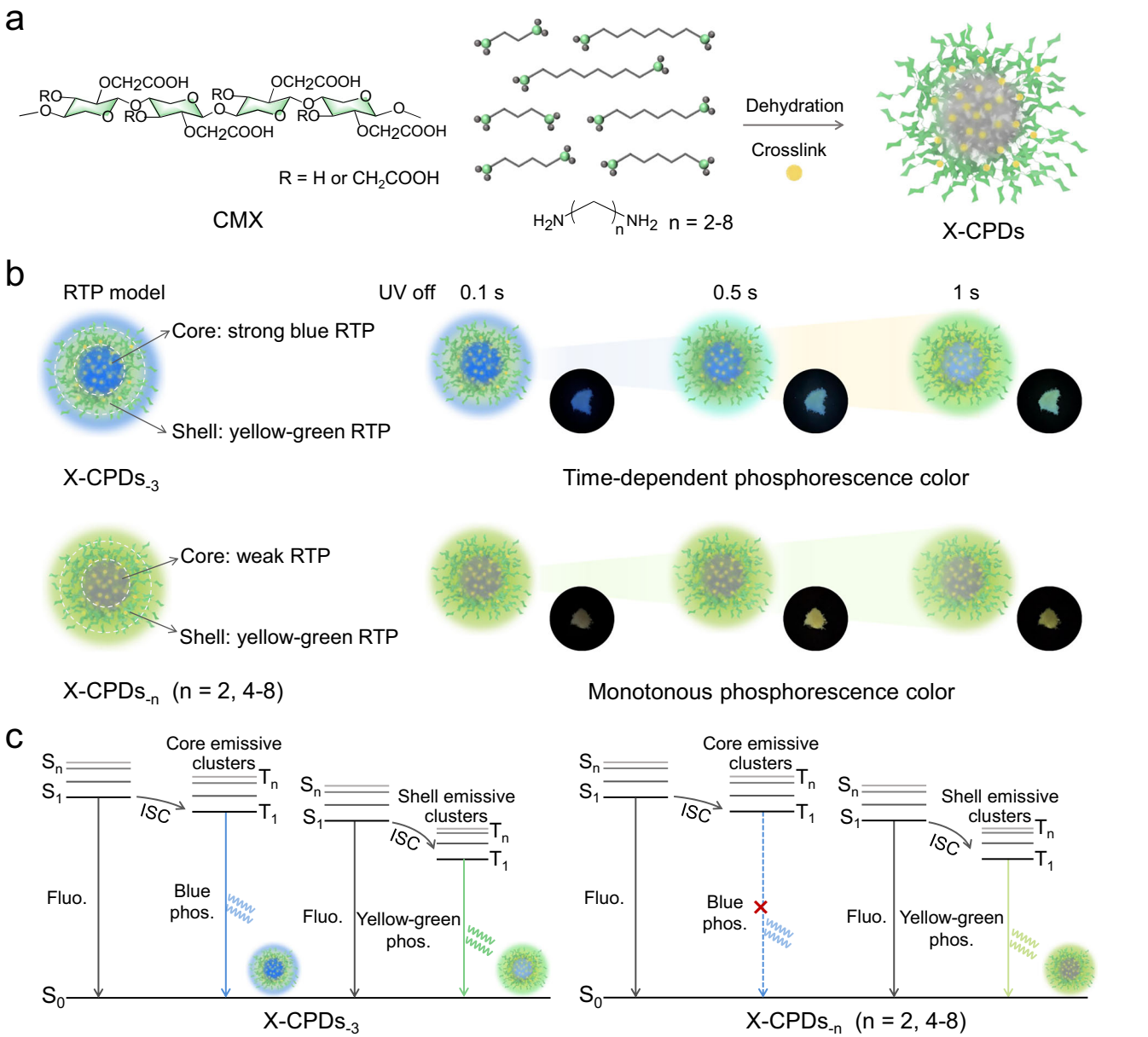

Fig. 1 | Strategy of TDPC in X-CPDs. a Schematic of the design strategy and hierarchical core-shell structure of the X-CPDs. **b** Schematic of the hierarchical luminescence center coupling and the origin of TDPC. **c** Mechanism for TDPC of X-CPDs$_{-3}$ under ambient conditions (Fluo.: fluorescence, phos.: phosphorescence).

C = O/C = N bonding, the peaks at 1395 cm^{-1} can be attributed to C-N vibrational, confirming the formation of amide/imide groups during cross-linking[2,44]. Moreover, the X-ray photoelectron spectroscopy (XPS) spectra were used to further study the surface structures of X-CPDs$_{-n}$ (n = 2–8). As shown in Figs. 2f, g and Supplementary Figs. 11–17, XPS spectra validate that X-CPDs$_{-n}$ (n = 2–8) all contain three elements of C, N, and O. The high-resolution C 1*s*, O 1*s*, and N 1*s* spectra of X-CPDs$_{-n}$ (n = 2–8) prove the presence of C-C/C = C, C-O/C-N, N-H, and C = O bonds, which are efficient to promote the spin–orbit coupling (SOC) and consequent ISC transitions (will discuss below). The above analysis results jointly indicate that X-CPDs$_{-n}$ (n = 2–8) feature the same bonding and functional group characteristics, the difference in RTP properties should come from the difference in microstructure and clusterization.

RTP properties of X-CPDs$_{-n}$

The photophysical properties of the as prepared X-CPDs$_{-n}$ (n = 2–8) were systematically investigated. As shown in Fig. 3a and Supplementary Fig. 18, after ceasing the 365 nm UV irradiation, X-CPDs$_{-n}$ (n = 2, 4–8) show yellow afterglows, lasting for 1.6–5 s. Notably, X-CPDs$_{-3}$ emits an obvious afterglow sustained for more than 6 s under ambient conditions. The delayed emission spectra of X-CPDs$_{-n}$ were used to identify the RTP properties (Fig. 3b). Obvious difference can be observed in the delayed emission. As shown in Fig. 3b, X-CPDs$_{-3}$ exhibit dual delayed emission peaks centered at 438 nm and 475 nm in the blue region due to the existence of inhomogeneous cluster emissive species, which can also be clearly recognized in the phosphorescence-excitation mapping of X-CPDs$_{-3}$ (Supplementary Fig. 19). As discussed above, there are abundant n → π* transition favored C = O/C = N groups and heteroatoms (N and O) in X-CPDs, which can also be verified by the UV-vis absorption spectra of CMX and X-CPDs (Supplementary Fig. 20 and Supplementary Discussion 1), thus, it is reasonable to suppose that N-related crosslinked core structure should be the cause of blue phosphorescence center in X-CPDs$_{-3}$. However, other X-CPDs$_{-n}$ (n = 2, 4–8) only exhibit broad emission peaks at ca. 550 nm in the yellow-green region, similar to

https://doi.org/10.1038/s41467-025-62807-6

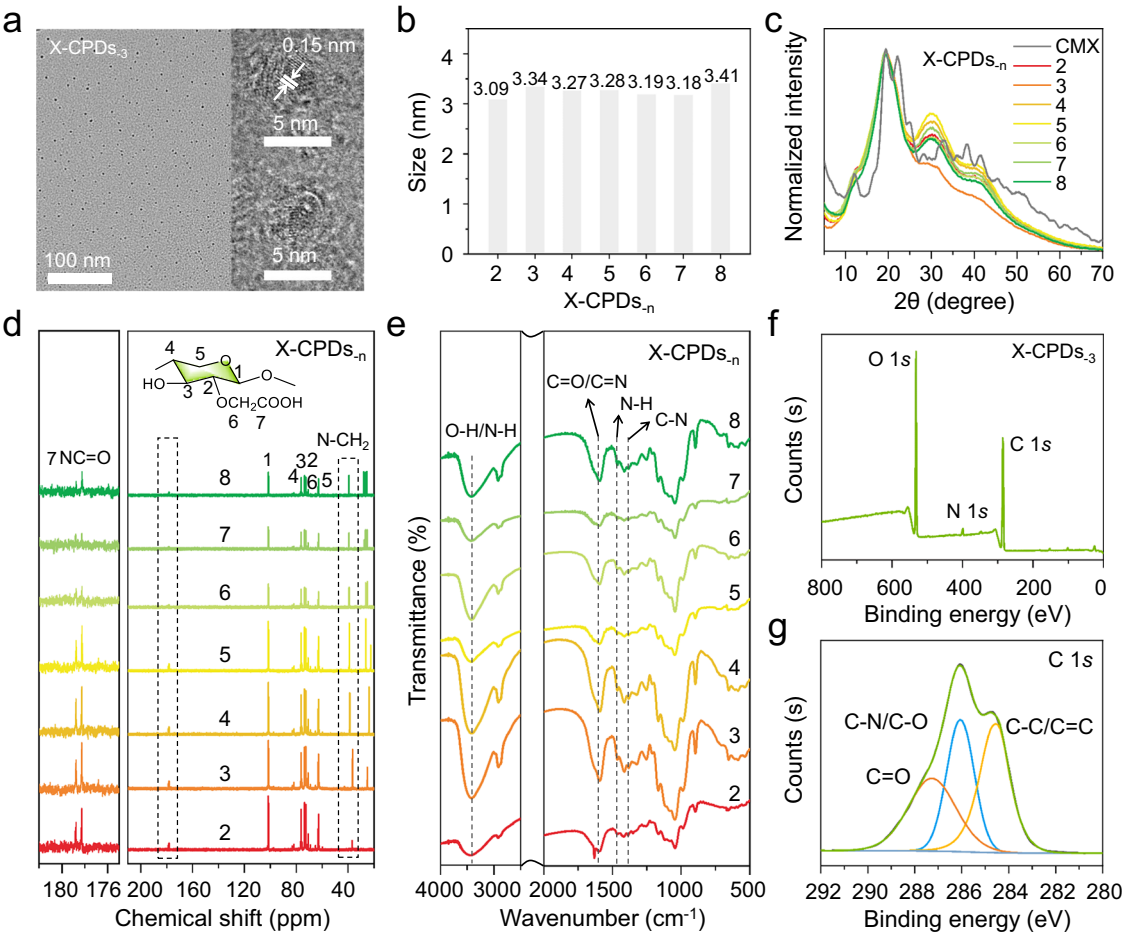

Fig. 2 | Characterization of X-CPDs-n. **a** TEM images of X-CPDs-3. **b** Size distributions of X-CPDs-n ($n = 2–8$). **c** XRD patterns of CMX and X-CPDs-n ($n = 2–8$). **d** ^{13}C NMR spectra of X-CPDs-n ($n = 2–8$) (500 MHz, D_2O). **e** FTIR spectra of X-CPDs-n ($n = 2–8$). **f** XPS survey spectra of X-CPDs-3. **g** High-resolution XPS C1*s* spectrum of X-CPDs-3.

CMX (Fig. 3b), indicating that the yellow-green phosphorescence of X-CPDs-n ($n = 2–8$) should originate from the low-energy surface oxide triplet state emissive clusters of CMX (Fig. 3a and Supplementary Fig. 21). The blue phosphorescence centers of X-CPDs-n ($n = 2, 4–8$) are not activated at room temperature. The Commission International de l'Eclairage (CIE) coordinate diagrams of X-CPDs-n ($n = 2–8$) are in good agreement with naked-eye observations (Fig. 3c), blue afterglow can only be observed in X-CPDs-3 at room temperature. As shown in Supplementary Fig. 22, the two emission peaks of X-CPDs-3 show a decreasing trend with the temperature increasing from 78 to 358 K, indicating the delayed emission peaks both belong to RTP. The phosphorescence decay curves of X-CPDs-n ($n = 2–8$) show that the RTP lifetimes are 162, 401, 387, 339, 314, 363 and 357 ms, respectively (Fig. 3d). Besides, the phosphorescence quantum yields of X-CPDs-n ($n = 2–8$) are calculated to be 0.07%, 6.46%, 0.96%, 0.7%, 0.18%, 0.15% and 0.2%, respectively (Fig. 3e). Thus, a comparative analysis reveals that X-CPDs-3 outperform other samples, with X-CPDs-2 demonstrates the lowest RTP performance.

Interestingly, further identification of the afterglow reveals that the afterglow color of X-CPDs-3 can evolve with time. Self-protective X-CPDs-3 exhibits TDPC from blue [UV off (t_{off}) = 0.1 s] via blue-green (t_{off} = 0.5 s) and then to yellow-green (t_{off} = 1 s) within 1 s after the excitation source is removed. Time-resolved emission spectrum (TRES) decay image of self-protective X-CPDs-3 was further mapped to monitor the TDPC behavior (Fig. 3f). The blue emission peak is the main component of the RTP at the moment of switching off the irradiation. As time goes by, the blue emission peaks located at ca. 438 nm and 475 nm gradually decrease and the yellow-green emission peaks located beyond 520 nm appear and gradually strengthen (Fig. 3g). The observed TDPC phenomenon in X-CPDs-3 arises from two well-separated emissive centers, where the yellow-green emission center exhibits a significantly longer phosphorescence lifetime (401 ms) compared to the blue emissive center (147 ms). The CIE coordinates of the afterglow visualize the dynamic color changing process, as shown in Fig. 3h, from which the marked colors are consistent with the naked-eye observation. More importantly, unlike previous studies employing petroleum-based polymers (e.g., polyacrylic acid) as precursors to prepare CPDs, where the polymer merely acts as a crosslinking skeleton without contributing to RTP due to its weak CTP effect. CMX used here exhibits strong CTP performance, enabling the CMX shell structure to emit yellow-green RTP. This innovative design of X-CPDs-3 facilitates the coexistence of core-shell dual phosphorescence centers in X-CPDs, thereby successfully achieving TDPC.

To exclude the influence of small molecular fluorophore substances on the RTP properties of the X-CPDs-3, several experiments were executed (Supplementary Figs. 23–29). The powerful evidence to exclude the RTP emission originates from small molecule fluorophore impurities is that the non-dialyzed X-CPDs-3 cannot emit RTP (Supplementary Figs. 23–24). There are low molecular weight impurities (such as amine substances and oligomers) in non-dialyzed X-CPDs-3 sample (Supplementary Figs. 25, 26), these impurities may disturb the emissive clusters and occur electron transfer interaction with X-CPDs-3, quenching the RTP, rather than contributing to RTP. Since X-CPDs are polymer structures, high performance gel permeation chromatography (HPGPC) test was then supplemented (Supplementary Fig. 27, Supplementary Table 1 and Supplementary Table 2).

https://doi.org/10.1038/s41467-025-62807-6

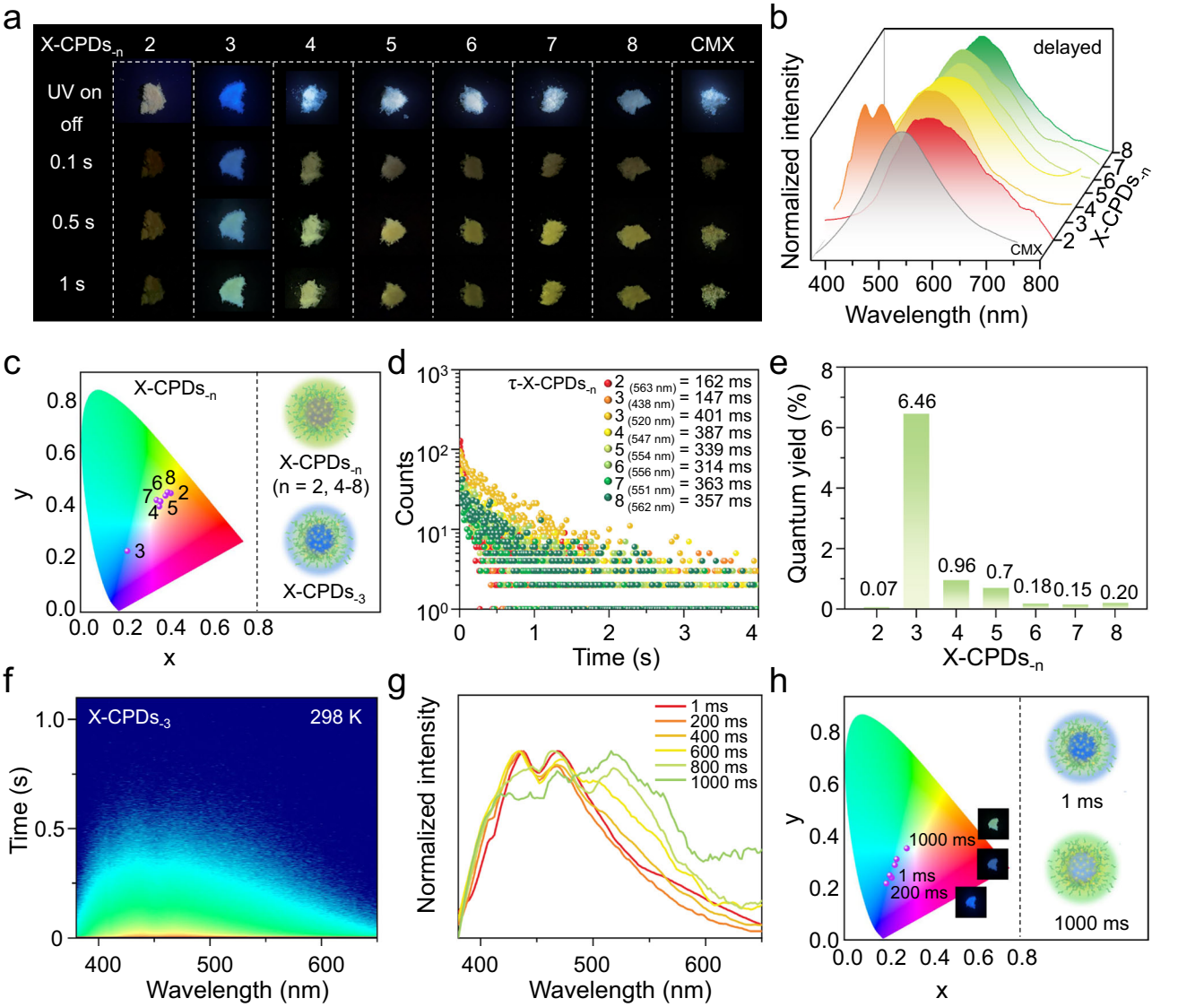

Fig. 3 | Photophysical properties of X-CPDs-n at room temperature. **a** Photographs of X-CPDs-n ($n = 2–8$) before and after turning off the UV lamp (365 nm) at room temperature. **b** Delayed emission spectra of CMX and X-CPDs-n ($n = 2–8$) (excitation wavelength: 365 nm, delay time: 1 ms). **c** The CIE coordinate diagrams plotted from the delayed spectra of X-CPDs-n ($n = 2–8$). **d** The phosphorescence lifetime decay curves of X-CPDs-n ($n = 2–8$). **e** Phosphorescence quantum yield of X-CPDs-n ($n = 2–8$). **f** Time-dependent phosphorescence mapping of X-CPDs-3 excited by 365 nm at room temperature. **g** Delayed emission spectra of X-CPDs-3 with varying delayed times excited by 365 nm at room temperature (interval of 200 ms). **h** Trajectory of TDPC of X-CPDs-3 in the CIE coordinate diagram at room temperature.

X-CPDs-3 is composed of three main components with different molecular weight ranges: 80–100 kDa, 5-8 kDa, and 1.6-1.9 kDa. X-CPDs-3 (50 kDa dialysis) has the highest ratio of 80-100 kDa components and the lowest ratio of 1.6–1.9 kDa components (Supplementary Table 1). X-CPDs-3 (50 kDa dialysis) has stronger RTP than X-CPDs-3 (1 kDa dialysis) and X-CPDs-3 (8 kDa dialysis), thus, 80–100 kDa high molecular weight components in X-CPDs-3 play a decisive role in the RTP performance (Supplementary Fig. 28). ^{1}H NMR spectra of X-CPDs-3 with high concentration and high scan number also show no characteristic signals belonging to fluorophore impurities (Supplementary Fig. 29). Taken together, the RTP observed in X-CPDs does not originate from small molecular fluorophore impurities, but originate from the hierarchical core–shell structure of X-CPDs-3.

Structure-TDPC performance relationship of X-CPDs

To figure out that why the TDPC can solely observed in X-CPDs-3, while not in other X-CPDs-n ($n = 2, 4–8$), a series of mechanism validation experiments were executed as follows. First, the effect of reaction conditions on TDPC was studied. X-CPDs-3 was prepared with different hydrothermal reaction time (2, 4, 6, 8, 10, 12 h) at 180 °C. X-CPDs-3-4h shows the most conspicuous TDPC phenomenon, and a blue-shifted phosphorescence CIE coordinate compared to other samples (Supplementary Figs. 30, 31). The enhanced blue phosphorescence originates from the fully exploited radiative transitions in the core of X-CPDs-3-4h. As discussed above, high-energy blue phosphorescence should come from the clusterization of N-related cross-linked core structure. The insufficient reaction time (i.e., 2 h) is detrimental to the formation of cross-linked core structures. While as the reaction time persistently increases (over 6 h), excessive carbonization and decline in N content also damages the clusterization of core structure (Supplementary Fig. 32). The delayed emission spectra and CIE coordinates show an enhancement of the yellow-green emission peak with increasing reaction time (Supplementary Fig. 31), confirming the deduction above.

To further support the viewpoint that N-related cross-linked core is responsible for the high-energy blue phosphorescence, different equivalent ratios of CMX and 1,3-diaminopropane are adopted to prepare X-CPDs$_{-3}$ (CMX: 1,3-diaminopropane = 3:1, 2:1, 1:1, 1:2, and 1:3, 180 °C for 4 h). The elemental analysis results show that the N content gradually increases with the increase of 1,3-diaminopropane (Supplementary Fig. 33). As a consequence, blue RTP progressively enhances with increasing of 1,3-diaminopropane (Supplementary Fig. 34), which are verified via the delayed spectra and CIE coordinates (Supplementary Fig. 35), again, stating the blue emissive center originates from N-related crosslinked structure. 1,3-diaminopropane analogs (1,2-propanediamine, n-propylamine) were also selected as cross-linker for contrast. Identical synthesis conditions were adopted to those used previously to ensure effective comparison and the corresponding products were donated as X-CPDs$_{-9}$ (1,2-propanediamine) and X-CPDs$_{-10}$ (n-propylamine). TEM images and XPS spectra indicate a similar morphology and structure features between X-CPDs$_{-3}$ and X-CPDs$_{-9}$ (Supplementary Figs. 36, 37). While the introduction of the methyl group in 1,2-propanediamine will increase the steric hindrance, obstructing the cross-linking and the CTP of cross-linked core (Supplementary Fig. 38). For X-CPDs$_{-10}$, the amine with a single reactive site cannot serve as an effective cross-linker to connect adjacent CMX chains (Supplementary Fig. 39). The elemental analysis results show the low nitrogen content of X-CPDs$_{-9}$ and X-CPDs$_{-10}$, verifying a low degree of cross-linking (Supplementary Fig. 40). Thus, X-CPDs$_{-9}$ and X-CPDs$_{-10}$ only reveal low-energy yellow-green RTP, and the lifetimes of which are reduced due to the obstructing of CEE and CTP effect (Supplementary Fig. 38 and Supplementary Fig. 41).

Since other X-CPDs$_{-n}$ (n = 2–8) all show analogical cross-linked core –shell structure, we wonder whether there are blue phosphorescence centers in these samples. The cryogenic test was subsequently executed, ultralow temperature can vastly suppress the nonradiative transition and distinctly exhibit the emissive ability of emissive clusters (i.e., blue phosphorescence center) which cannot be observed at room temperature (Fig. 4a, Supplementary Figs. 42, 43). Indeed, the phosphorescence lifetimes of X-CPDs$_{-n}$ (n = 2–8) are vastly boosted to 1061, 3637, 3045, 3412, 2852, 1989, and 2036 ms at 77 K, respectively (Fig. 4b). Surprisingly, when cooled to 77 K, X-CPDs$_{-n}$ (n = 2–8) all exhibit TDPC, ending with blue-green or blue afterglows, allowing the blue emissive centers to be activated (Fig. 4a and Supplementary Fig. 42). However, CMX precursor has no blue phosphorescence at 77 K, proving that the crosslinked structure should be responsible for the blue emissive center in X-CPDs$_{-n}$ (n = 2–8) (Fig. 4a and Supplementary Fig. 42). Taking the X-CPDs$_{-3}$ and X-CPDs$_{-4}$ as examples, which were selected for TRES testing at 77 K (Fig. 4c–h). The emissive ability of the blue emissive centers in X-CPDs$_{-3}$ and X-CPDs$_{-4}$ are fully exhibited at ultralow temperature. As shown in Fig. 4d and Fig. 4g, the delayed spectra of X-CPDs$_{-3}$ and X-CPDs$_{-4}$ show a blue shift trend over time, which are consistent with the change in afterglow. The color variations of X-CPDs$_{-3}$ and X-CPDs$_{-4}$ are marked in CIE coordinates (Fig. 4e and Fig. 4h), which are also consistent with the naked-eye observation. Thus, it could be concluded that high-energy N-related blue phosphorescence centers are existing in both X-CPDs$_{-3}$ and X-CPDs$_{-n}$ (n = 2, 4–8). The distinction resides in the room-temperature activation of blue phosphorescence centers of X-CPDs$_{-3}$, whereas those in other X-CPDs$_{-n}$ (n = 2, 4–8) require low-temperature conditions (e.g., 77 K) (Fig. 4i).

The longer alkyl chains in X-CPDs$_{-n}$ (n = 4–8) allow greater vibrational and rotational freedom, weakening the CEE effect of the cross-linked network, thus, the blue phosphorescence centers are not rigid enough to emit at room temperature. As for X-CPDs$_{-2}$, the shorter alkyl chain results in less steric hindrance, and the reaction sites are close to each other, making it easier to carbonization, which can be verified by the UV-vis absorption spectra[47,48] (Supplementary Fig. 20, Supplementary Figs. 44–46 and Supplementary Discussion 2). Excessive carbonization will disturb the CEE effect and interfere CTP, thus, X-CPDs$_{-2}$ exhibits the worst RTP performance in terms of phosphorescence lifetime and quantum yield among X-CPDs$_{-n}$ (n = 2–8). To sum up, by precisely modulating the length of diamine, the core–shell hierarchical structure of X-CPDs can activate multiple emissive centers and lead to a typical TDPC evolution.

Applications of X-CPDs$_{-n}$

Based on the interesting TDPC performance of X-CPDs$_{-3}$, several potential applications were designed. X-CPDs$_{-n}$ can be dispersed in epoxy resin and cured to prepare 3D anti-counterfeiting artefacts (Fig. 5a, Supplementary Figs. 47–49 and Supplementary Discussion 3). With the help of a mold, we prepared artefacts in the shape of a love heart with a vivid afterglow using X-CPDs$_{-3}$ and X-CPDs$_{-6}$ (Fig. 5a). As shown in Fig. 5b, love heart prepared by X-CPDs$_{-6}$ exhibits static yellow-green afterglow, while love heart prepared by X-CPDs$_{-3}$ exhibits TDPC from blue to blue-green then to yellow-green. Love hearts were then assembled into shamrock shapes for an intriguing structural afterglow, the top of shamrock afterglow can evolve with time while the bottom shows monotonous afterglow. Furthermore, a variety of good-looking crafts can be prepared by X-CPDs$_{-n}$ and epoxy resin, such as mushroom, lucky bag, chain hoist, stars, starfish, dolphins, and so on (Fig. 5c and Supplementary Fig. 50). For instance, after ceasing the 365 nm UV irradiation, mushroom prepared by X-CPDs$_{-6}$ exhibits monotonous yellow-green phosphorescence. As a comparison, mushroom prepared by X-CPDs$_{-3}$ shows TDPC (Fig. 5d). Due to the protection of epoxy resin, they also show water-resistant performance and can emit afterglows under water.

X-CPDs$_{-n}$ with different phosphorescence lifetimes also show great potential for complex data encryption. A dot-matrix (4 × 8) groove is fabricated by X-CPDs$_{-3}$, X-CPDs$_{-8}$, and a blue fluorescence dye without RTP, to perform proof-of-concept experiment (Fig. 5e). A conventional logic gate suitable for the time-resolved encryption of monochromatic messages is known as Pathway I. In this system, the signals 1 and 0 are used to indicate the emitting and disappearing states of the dots, respectively. When excited by 365 nm UV light, all dots exhibit strong blue fluorescence, corresponding to an invalid binary code. Once the excitation source is stopped, the spatial-resolved binary codes appear at 0.1 and 0.5 s, resulting in the misleading message RBHC based on ASCII (American Standard Code for Information Interchange) code. While as time-prolonged at 5.0 s, the binary code is decoded as 2280 based on decimal numbers. However, only error information can be obtained through Pathway I, and the correct information must be obtained through pathway II decoding. The TDPC of X-CPDs$_{-3}$ in pathway II can provide new channels (1 + 1 = 10 (0 carries 1 in binary)) to enhance the security of data encryption. When the spatial-resolved binary codes appear at 0.5 s, the correct information TDPC can be obtained basis on ASCII, which is used to illustrate the importance of TDPC performance in the field of advanced data encryption. However, the information 2(2280) basis on decimal numbers is twice of 2280 in pathway I. This number is used to indicate that the information obtained the second time in pathway II is the correct information. The demonstration results show that the introduction of materials with TDPC performance into the matrix system can effectively increase the load capacity of the information and enhance the security of the decryption process.

In summary, a hierarchical luminescence center coupling strategy is developed to endow self-protective CPDs with TDPC. X-CPDs$_{-n}$ (n = 2–8) are synthesized through the dehydration and crosslinking reaction between CMX and various alkyl diamines. Thanks to the rigid environment provided by hydrogen bonding and covalent bonds formed by cross-linking, self-protective X-CPDs$_{-n}$ (n = 2–8) can realize RTP via CTP. By precisely modulating the structure of the cross-linked core, the blue phosphorescence of X-CPDs$_{-3}$ is fully released at ambient conditions. Thus, the core-related blue phosphorescence center and shell-related yellow-green phosphorescence center coexist in

https://doi.org/10.1038/s41467-025-62807-6

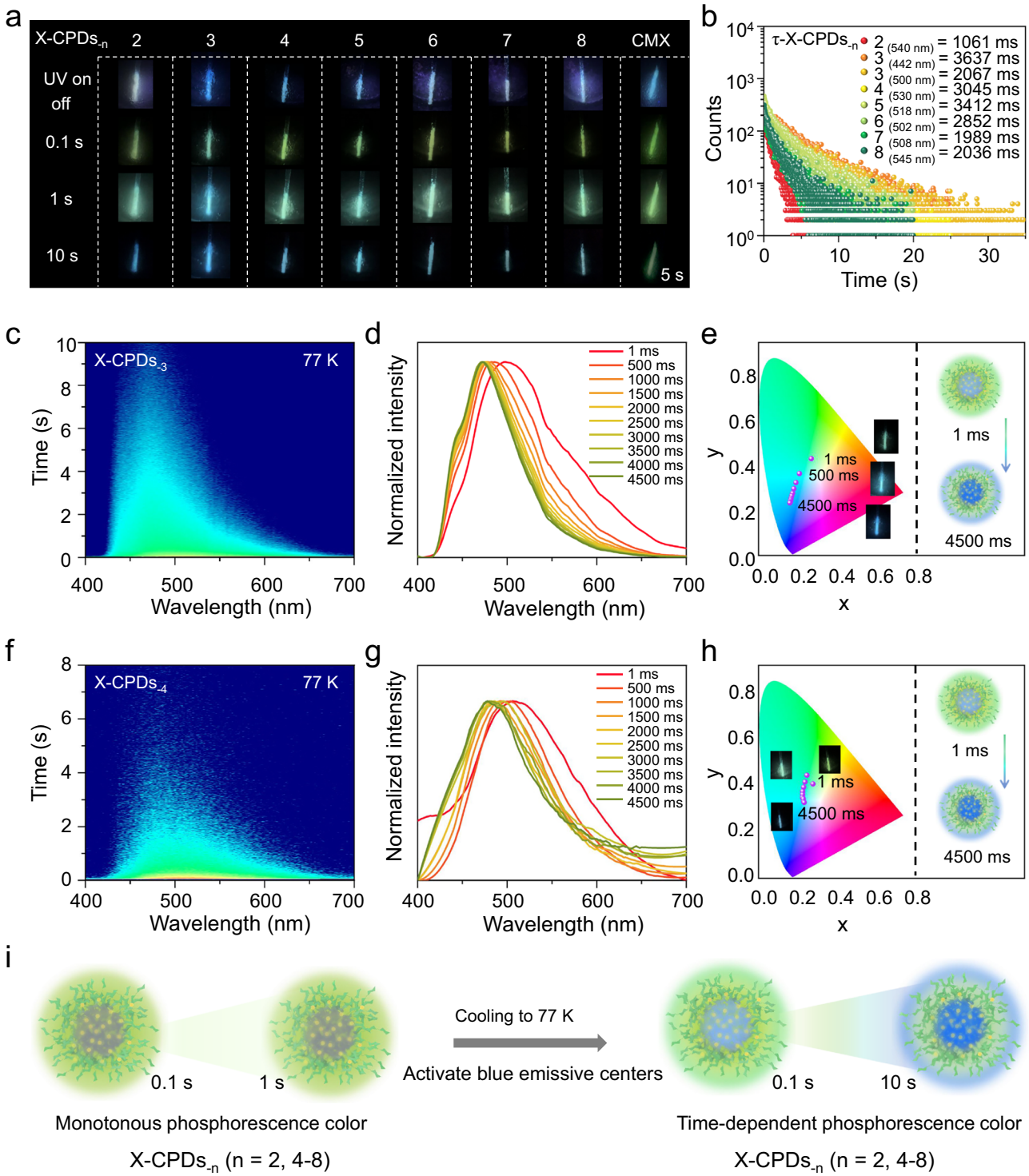

Fig. 4 | Photophysical properties of X-CPDs-n at 77 K. a Photographs of X-CPDs-n (n = 2–8) before and after turning off the UV lamp (365 nm) at 77 K. **b** The phosphorescence lifetime decay curves of X-CPDs-n (n = 2–8) at 77 K. **c**, **f** Time-dependent phosphorescence mapping of (**c**) X-CPDs-3 or (**f**) X-CPDs-4 excited by 365 nm at 77 K. **d**, **g** Delayed emission spectra of (**d**) X-CPDs-3 or (**g**) X-CPDs-4 with varying delayed times excited by 365 nm at 77 K (interval of 500 ms). **e**, **h** Trajectory of TDPC of (**e**) X-CPDs-3 or (**h**) X-CPDs-4 in the CIE coordinate diagram at 77 K. **i** Schematic of the formation of TDPC of the X-CPDs-n (n = 2, 4–8).

X-CPDs-3, realizing high contrast TDPC without any matrix confinement nor multicomponent doping. X-CPDs-3 with TDPC and X-CPDs-n (n = 2–8) with different phosphorescence lifetimes can be applied in advanced dynamic information encryption and anti-counterfeiting. This work not only provides an effective method for self-protective CPDs to achieve TDPC, but also provides insights into the phosphorescence mechanism of CPDs.

Methods

Materials

Industrial xylan was obtained from a viscose fiber mill in Sichuan Yibin (China), and was dialyzed to remove excessive salts. Ethylenediamine (EDA) (99%), 1,3-diaminopropane (98%), 1,4-diaminobutane (98%), 1,5-diaminopentane (97%), 1,6-diaminlhexane (98%), 1,7-diaminoheptane (98%), 1,8-diaminooctane (98%), and

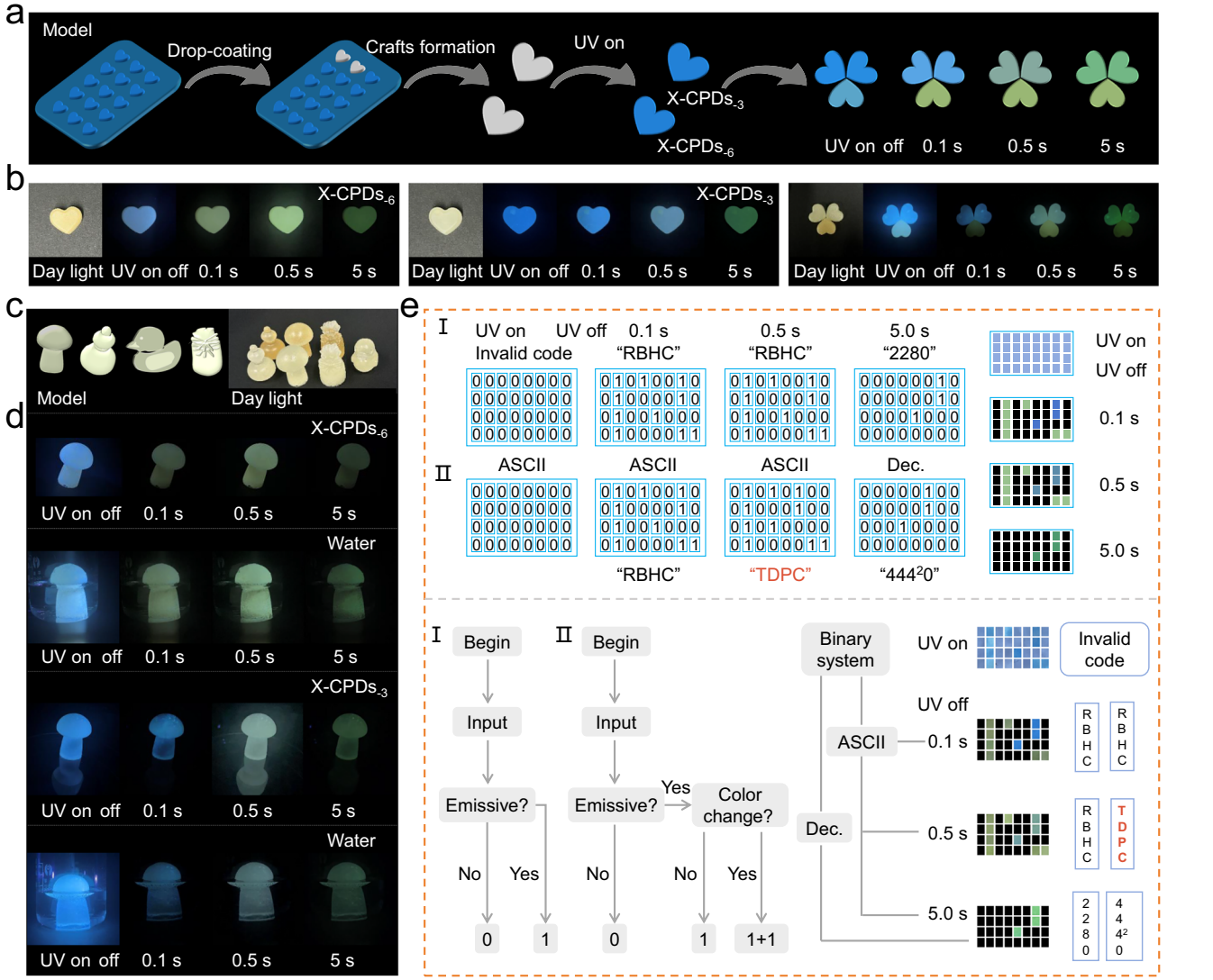

Fig. 5 | Practicability of X-CPDs$_{-n}$ RTP materials. a Demonstration of anticounterfeiting applications using the artefacts consisting of varying X-CPDs$_{-n}$. **b** The afterglows of shamrock prepared by X-CPDs$_{-6}$ and X-CPDs$_{-3}$ after ceasing the 365 nm UV light excitation. **c** Handicrafts prepared by X-CPDs$_{-n}$ and epoxy resin. **d** The afterglow comparison of handicrafts with or without TDPC. **e** Demonstration of dynamic encryption based on time-resolved (I) and time-color-resolved (II) encryption.

1,2-propanediamine (99%) were purchased from Macklin Chemistry Co. Ltd (Shanghai, China). N-propylamine (98%) was purchased from Energy Chemical. All the used reagents were analytical grade without further purification.

Synthesis of CMX

CMX was synthesized according to the previous method[42]. Initially, 5 g of xylan was dispersed in 40 mL of 2% NaOH solution under continuous stirring. This mixture was maintained at 60 °C for half an hour. Subsequently, 5.824 g of $ClCH_2COOH$ was introduced into the reaction system, after which the temperature was increased to 65 °C and held constant for 70 min. Following the reaction, the resulting product was neutralized using diluted acetic acid and subjected to multiple ethanol washes for purification. The final product, CMX, was obtained by drying under vacuum at 50 °C for 6 h. The degree of substitution of CMX was determined to be 0.32.

Synthesis of X-CPDs$_{-n}$

CMX (450 mg) was dissolved in deionized water (10 mL). After that, diamines (EDA (180.3 mg, 3 mmol), 1,3-diaminopropane (222.4 mg, 3 mmol), 1,4-diaminobutane (264.5 mg, 3 mmol), 1,5-diaminopentane (306.5 mg, 3 mmol), 1,6-diaminlhexane (348.6 mg, 3 mmol), 1,7-diaminoheptane (390.7 mg, 3 mmol), 1,8-diaminooctane (432.8 mg, 3 mmol), 1,2-propanediamine (222.4 mg, 3 mmol), n-propylamine (177.3 mg, 3 mmol)) were added and mixed uniformly. Then, the mixed solutions were transferred into a Teflon-lined autoclave and heated at 180 °C for 4 h in oven. After dialysis and freeze-drying, the solid samples were obtained, namely, X-CPDs$_{-2}$, X-CPDs$_{-3}$, X-CPDs$_{-4}$, X-CPDs$_{-5}$, X-CPDs$_{-6}$, X-CPDs$_{-7}$, X-CPDs$_{-8}$, X-CPDs$_{-9}$, and X-CPDs$_{-10}$, respectively.

Synthesis of X-CPDs$_{-3}$ with different reaction times

The synthesis procedure was the same as above, except for the reaction time which was set as 2 h, 6 h, 8 h, 10 h, and 12 h.

Synthesis of X-CPDs$_{-3}$ with different equivalent ratios

The synthesis procedure was the same as above, except for the equivalent ratio (CMX:1,3-diaminopropane) which was set as 3:1 (450 mg:74.1 mg), 2:1 (450 mg:111.2 mg), 1:2 (450 mg:444.8 mg), and 1:3 (450 mg:667.2 mg).

Synthesis of X-CPDs-3 with different dialysis treatment

To exclude the influence of small molecular fluorophore substances on the RTP properties of the X-CPDs-3, dialysis bags of different molecular weights cutoff of 1 kDa, 8 kDa, and 50 kDa were used to purify the samples[49].

Data availability

All relevant data are included in this Article and Supplementary Information. Data are available from the corresponding author upon request.

References

1. An, Z. et al. Stabilizing triplet excited states for ultralong organic phosphorescence. *Nat. Mater.* **14**, 685–690 (2015).
2. Tao, S. et al. Design of metal-free polymer carbon dots: a new class of room-temperature phosphorescent materials. *Angew. Chem. Int. Ed.* **57**, 2393–2398 (2018).
3. Gao, Q., Lü, B. & Peng F. Natural polysaccharide-based room-temperature phosphorescence materials: designs, properties, and applications. *Prog. Mater. Sci.* **148**, 101372 (2024).
4. Shi, H. et al. Ultralong organic phosphorescence: from material design to applications. *Acc. Chem. Res.* **55**, 3445–3459 (2022).
5. Chen, Y., Wang, S. & Zhang, F. Near-infrared luminescence high-contrast in vivo biomedical imaging. *Nat. Rev. Bioeng.* **1**, 60–78 (2023).
6. Baryshnikov, G., Minaev, B. & Ågren, H. Theory and calculation of the phosphorescence phenomenon. *Chem. Rev.* **117**, 6500–6537 (2017).
7. He, Z. et al. Achieving persistent, efficient, and robust room-temperature phosphorescence from pure organics for versatile applications. *Adv. Mater.* **31**, 1807222 (2019).
8. Wu, P. et al. 3D printed room temperature phosphorescence materials enabled by edible natural konjac glucomannan. *Adv. Mater.* **36**, 2402666 (2024).
9. Kabe, R., Notsuka, N., Yoshida, K. & Adachi, C. Afterglow organic light-emitting diode. *Adv. Mater.* **28**, 655–660 (2016).
10. Lou, Q. et al. Thermally enhanced and long lifetime red TADF carbon dots via multi-confinement and phosphorescence assisted energy transfer. *Adv. Mater.* **35**, 2211858 (2023).
11. Gao, Q. et al. Large-scale preparation for multicolor stimulus-responsive room-temperature phosphorescence paper via cellulose heterogeneous reaction. *Adv. Mater.* **35**, 2305126 (2023).
12. Liu, Y. et al. Carbon dots-inked paper with single/two-photon excited dual-mode thermochromic afterglow for advanced dynamic information encryption. *Adv. Mater.* **36**, 2403775 (2024).
13. Gu, L. et al. Colour-tunable ultra-long organic phosphorescence of a single-component molecular crystal. *Nat. Photonics* **13**, 406–411 (2019).
14. Liu, S., Fang, X., Lu, B. & Yan, D. Wide range zero-thermal-quenching ultralong phosphorescence from zero-dimensional metal halide hybrids. *Nat. Commun.* **11**, 4649 (2020).
15. Fermi, A., Bergamini, G., Roy, M., Gingras, M. & Ceroni, P. Turn-on phosphorescence by metal coordination to a multivalent terpyridine ligand: a new paradigm for luminescent sensors. *J. Am. Chem. Soc.* **136**, 6395–6400 (2014).
16. Li, Y. et al. Activatable red/near-infrared aqueous organic phosphorescence probes for improved time-resolved bioimaging. *Nat. Sci. Rev.* **12**, nwae383 (2025).
17. Zhao, Y. et al. Fused-ring pyrrole-based near-infrared emissive organic RTP material for persistent afterglow bioimaging. *Angew. Chem. Int. Ed.* **63**, e202317431 (2024).
18. Chen, T. & Yan, D. Full-color, time-valve controllable and Janus-type long-persistent luminescence from all-inorganic halide perovskites. *Nat. Commun.* **15**, 5281 (2024).
19. Li, W. et al. A universal strategy for activating the multicolor room-temperature afterglow of carbon dots in a boric acid matrix. *Angew. Chem. Int. Ed.* **58**, 7278–7283 (2019).
20. Ju, H. et al. Polymerization-induced crystallization of dopant molecules: an efficient strategy for room-temperature phosphorescence of hydrogels. *J. Am. Chem. Soc.* **145**, 3763–3773 (2023).
21. Wang, T. et al. Recent advances in long-persistent luminescence materials based on host–guest architecture. *Chin. Chem. Lett.* **35**, 108385 (2024).
22. Li, S. et al. Regulation of thermally activated delayed fluorescence to room-temperature phosphorescent emission channels by controlling the excited-states dynamics via J- and H-aggregation. *Angew. Chem. Int. Ed.* **60**, 18059–18064 (2021).
23. Wang, P. et al. Producing long afterglow by cellulose confinement effect: a wood-inspired design for sustainable phosphorescent materials. *Carbon* **171**, 946–952 (2021).
24. Xing, C., Qi, Z., Zhou, B., Yan, D. & Fang, W.-H. Solid-state photochemical cascade process boosting smart ultralong room-temperature phosphorescence in bismuth halides. *Angew. Chem. Int. Ed.* **63**, e202402634 (2024).
25. Wu, H. et al. Achieving amorphous ultralong room temperature phosphorescence by coassembling planar small organic molecules with polyvinyl alcohol. *Adv. Funct. Mater.* **29**, 1807243 (2019).
26. Gao, Q. et al. Fully exploiting clusterization-triggered room temperature phosphorescence of cellulose by stepwise rigidification for long-lived and excitation wavelength-dependent afterglows. *Adv. Funct. Mater.* **34**, 2403977 (2024).
27. Lü, B. et al. Natural ultralong hemicelluloses phosphorescence. *Cell Rep. Phys. Sci.* **3**, 101015 (2022).
28. Wang, J.-X. et al. Time-dependent afterglow color in a single-component organic molecular crystal. *Angew. Chem. Int. Ed.* **59**, 10032–10036 (2020).
29. Wang, Z. et al. Four-in-one stimulus-responsive long-lived luminescent systems based on pyrene-doped amorphous polymers. *Angew. Chem. Int. Ed.* **61**, e202203254 (2022).
30. Wang, Z. et al. Color-tunable polymeric long-persistent luminescence based on polyphosphazenes. *Adv. Mater.* **32**, 1907355 (2020).
31. Chen, T., Ma, Y.-J. & Yan, D. Single-component 0d metal–organic halides with color-variable long-afterglow toward multi-level information security and white-light LED. *Adv. Funct. Mater.* **33**, 2214962 (2023).
32. Wang, D. et al. Achieving color-tunable and time-dependent organic long persistent luminescence via phosphorescence energy transfer for advanced anti-counterfeiting. *Adv. Funct. Mater.* **33**, 2208895 (2023).
33. Kang, C. et al. Enabling carbonized polymer dots with color-tunable time-dependent room temperature phosphorescence through confining carboxyl dimer association. *Angew. Chem. Int. Ed.* **63**, e202316527 (2024).
34. Sun, J. et al. Enabling controllable time-dependent phosphorescence in carbonized polymer dots based on chromophore excited triplet energy level modulation by ionic bonding. *Angew. Chem. Int. Ed.* **64**, e202415042 (2025).
35. Shi, W. et al. Time-dependent phosphorescence color of carbon dots in binary salt matrices through activations by structural confinement and defects for dynamic information encryption. *Angew. Chem. Int. Ed.* **62**, e202303063 (2023).
36. Yang, T. et al. Time-dependent afterglow from a single component organic luminogen. *Research* **59**, 10032–10036 (2021).
37. Tan, J. et al. Time-dependent phosphorescence colors from carbon dots for advanced dynamic information encryption. *Adv. Mater.* **33**, 2006781 (2021).
38. Jiang, K., Wang, Y., Gao, X., Cai, C. & Lin, H. Facile, quick, and gram-scale synthesis of ultralong-lifetime room-temperature-

phosphorescent carbon dots by microwave irradiation. *Angew. Chem. Int. Ed.* **57**, 6216–6220 (2018).
39. Sun, Y. et al. Ultralong lifetime and efficient room temperature phosphorescent carbon dots through multi-confinement structure design. *Nat. Commun.* **11**, 5591 (2020).
40. Wang, B., Waterhouse, G. I. N., Yang, B. & Lu, S. Advances in shell and core engineering of carbonized polymer dots for enhanced applications. *Acc. Chem. Res.* **57**, 2928–2939 (2024).
41. Chen, J. et al. Dynamic room temperature phosphorescence of silane-functionalized carbon dots confining within silica for anti-counterfeiting applications. *Small* **20**, 2306323 (2024).
42. Shi, M. et al. Confinement-modulated clusterization-triggered time-dependent phosphorescence color from xylan-carbonized polymer dots. *J. Am. Chem. Soc.* **146**, 1294–1304 (2024).
43. Ren, J.-L., Peng, F. & Sun, R.-C. Preparation and characterization of hemicellulosic derivatives containing carbamoylethyl and carboxyethyl groups. *Carbohyd. Res.* **343**, 2776–2782 (2008).
44. Song, S.-Y. et al. Self-exothermic reaction driven large-scale synthesis of phosphorescent carbon nanodots. *Nano Res.* **14**, 2231–2240 (2021).
45. Duan, P., Zhi, B., Coburn, L., Haynes, C. L. & Schmidt-Rohr, K. A molecular fluorophore in citric acid/ethylenediamine carbon dots identified and quantified by multinuclear solid-state nuclear magnetic resonance. *Magn. Reson. Chem.* **58**, 1130–1138 (2020).
46. Tao, S. et al. Confined-domain crosslink-enhanced emission effect in carbonized polymer dots. *Light.: Sci. Appl.* **11**, 56 (2022).
47. Song, Y. et al. Investigation from chemical structure to photoluminescent mechanism: a type of carbon dots from the pyrolysis of citric acid and an amine. *J. Mater. Chem. C.* **3**, 5976–5984 (2015).
48. Feng, T. L. et al. Color-tunable carbon dots possessing solid-state emission for full color light-emitting diodes applications. *ACS Photonics* **5**, 502–510 (2018).
49. Essner, J. B., Kist, J. A., Polo-Parada, L. & Baker, G. A. Artifacts and errors associated with the ubiquitous presence of fluorescent impurities in carbon nanodots. *Chem. Mater.* **30**, 1878–1887 (2018).

Acknowledgements

This work was supported by the National Science Fund for Distinguished Young Scholars of China (32225034) (P.F.), the National Natural Science Foundation of China (22308028) (L.B.), the Fundamental Research Funds for the Central Universities (JCYJ202501) (L.B.), the National Key Research and Development Program of China (NO. 2024YFD2200804) (L.B.), the Young Elite Scientists Sponsorship Program by CAST (YESS20240208) (L.B.). The authors would like to thank the Innovation Platform for High-Value Utilization of Forest Resources at Beijing Forestry University for supporting the XPS equipment resources.

Author contributions

S.M. and L.B. designed the experiments. S.M. carried out the experiments. G. Q. and C.M. contributed to optical characterizations. L.Z. contributed to structural characterizations. R.J. (Jun Rao), C.G., Q.W., and R.J. (Junli Ren) contributed to helpful discussion. S.M. and L.B. wrote the original manuscript and revised the manuscript. L.B. and P.F. supervised the project.

Competing interests

The authors declare no competing interests.

Additional information

Supplementary information The online version contains supplementary material available at https://doi.org/10.1038/s41467-025-62807-6.

Correspondence and requests for materials should be addressed to Baozhong Lü or Feng Peng.

Peer review information *Nature Communications* thanks Changlong Jiang and the other, anonymous, reviewers for their contribution to the peer review of this work. A peer review file is available.